Modeling of Bearing Voltage in Electric Machines Based on Electromagnetic FEA and Measured Bearing Capacitance

Peng Han, *Senior Member, IEEE,* Greg Heins, *Member, IEEE,* Dean Patterson, *Life Fellow, IEEE,* Mark Thiele, *Member, IEEE,* and Dan M. Ionel, *Fellow, IEEE*

Abstract—Bearing voltages and associated bearing currents in electric machines driven by pulse width modulation (PWM) converters with high switching frequencies and high dv/dt can cause premature bearing failures. This paper proposes a new modeling approach for the prediction of steady-state and transient bearing voltages based on 2-dimensional (2D) electromagnetic finite element analysis (FEA) with coupled external circuits using measured bearing capacitance values. The distributed-element external circuit was employed mainly to take into account the influence of wire distribution and frequency dependency, which are typically neglected by traditional equivalent circuits. The developed model was then used to simulate bearing voltages for various scenarios and evaluate the effectiveness of several easy-to-implement bearing voltage reduction methods from the perspective of machine design and manufacturing, such as using the insulated shaft and/or bearings, introducing additional insulation in the rotor, and changing the material of machine components. Experimental measurements are also provided to facilitate the analysis and validate the proposed approach.

Index Terms—Bearing current, bearing voltage, capacitance, electric machine, insulated bearing, insulated shaft, PWM converter.

I. INTRODUCTION

Bearing failures in electric machines and electric machine-driven equipment are attributed to mechanical/thermal causes or bearing currents. Shaft voltages and the resulting bearing currents in line-operated electric machines are mainly produced by the homopolar flux, magnetic asymmetry or electrostatic effect. During the past decades, with the proliferation of variable speed drives using pulse width modulation (PWM) voltage source inverters, a growing number of bearing current induced premature bearing failures have been reported, calling for more research effort into bearing currents and the associated mitigation techniques [1–4]. More recently, advanced wide band gap (WBG) devices based machine drives with much higher switching frequencies ranging from a few hundreds of kHz to MHz and higher dv/dt pose new challenges for bearing reliability [5].

It has been well known that all the rotating machines potentially have bearing current issues, either of large or small horsepowers [1]. Small inverter-fed ac machines are likely to suffer from electrical discharge machining bearing currents, and larger machines are likely to be exposed to high-frequency circulating bearing currents [6].

The voltage across the bearing lubricant film, i.e., the bearing voltage V_b, can be built up by the electrostatic charge accumulation, the common mode voltage (CMV) through capacitive coupling, and the common mode current or magnetic asymmetry through inductive coupling. The bearing current will flow and damage the surface of bearing raceways once the instantaneous bearing voltage exceeds a given threshold value [1].

Main bearing current types include: the localized current induced by homopolar fringing magnetic fluxes, the leakage current to the ground, the non-circulating type caused by the shaft-to-frame voltage and the circulating type introduced by the shaft end-to-end voltage [7]. The bearing voltage is typically used as an indicator of bearing failures since both the non-circulating and circulating bearing currents are closely related to the potential drop across the bearing [2, 4]. The accurate prediction of bearing voltage and cost-effective mitigation solutions are important topics in this research area, such as the recent work presented in [8, 9].

The accuracy of the bearing voltage prediction in steady state relies heavily on bearing and machine capacitances. Capacitances between machine components, such as the stator-winding-to-rotor capacitance C_{sr}, stator-winding-to-frame capacitance C_{sf} and rotor-to-frame capacitance C_{rf}, can be estimated by analytical equations [10, 11] or calculated by electrostatic finite element (FE) solvers based on accurate CAD files [12]. The prediction of bearing voltage transients involves not only capacitances, but also the high-frequency RL parameters related to machine windings. The frequency-dependent resistances and inductances can be extracted by solving eddy current problems or directly modeled in time-stepping (transient) electromagnetic FE analysis (FEA).

The bearing voltage has traditionally been modeled by various types of equivalent circuits [13]. The simple capacitive lumped-element equivalent circuit (LEC), alternatively termed as the capacitive voltage divider, was mainly used to estimate the steady-state bearing voltage and define the bearing voltage ratio [7]. By adding some lumped zero-sequence impedances, the simple equivalent circuit, i.e., the common-mode equivalent circuit, has been used to simulate the bearing current [1, 14, 15].

In order to further consider the frequency dependency of the winding impedance, more detailed lumped-element circuits were proposed and their parameters were typically extracted by the common mode and differential mode impedance measurements [16, 17]. The distributed-element equivalent circuits (DECs) were mainly used for the frequency-domain analysis of electromagnetic interference (EMI) [18] and time-domain voltage stress prediction [19–21] but rarely seen in studies of bearing voltages.

This paper makes an attempt to apply the electromagnetic FEA with coupled distributed-element circuits to directly predict the bearing voltage in the time domain, taking into account the influence of the placement of in-slot wires, frequency dependency of winding resistance and inductance parameters

due to the skin effect. The proposed model maintains the highest fidelity of the machine construction and is easy to set up with no need to extract and assign the frequency-dependent resistance and inductance parameters.

The calculation of bearing capacitance has also been studied in the existing literature. Equations based on Hertizian contact theory were presented to calculate capacitances of roller and ball bearings in large induction motors under radial loads [22]. Bearing capacitances under various operating conditions were measured and used to back-calculate the lubricant film thickness [23]. The starvation effect for grease lubricant has also been experimentally identified, which can be explained by the fact that there is insufficient grease flowing back to the entry point between two rollover processes at high speeds and the lubricant film thickness is thus significantly reduced. Recent work on bearing current and shaft voltage predictions mainly used measured bearing capacitances, whereas the variations in temperature, speed and load were not considered thoroughly [8, 11].

This paper extends the conference papers [24] and [25] with enhanced simulation studies and experimental validations. The new modeling approach for the prediction of transient and steady-state bearing voltages in electric machines, which combines the electromagnetic FEA with detailed external circuits, is the main contribution. The second contribution is the combined numerical and experimental method for the determination of bearing capacitances, taking into account the uncertainty factors of steel ball bearing products. The third main contribution is the evaluation of potential bearing voltage reduction approaches, i.e., using insulated shaft and/or bearings, introducing additional insulation and changing the material of motor components, aiming to provide best design practices for real industry implementations.

This paper is organized as follows. Section II shows the DEC representation of electric machines for bearing voltage study, taking into account the distribution and high-frequency effect of winding turns. Section III shows the extraction of machine-related capacitances from electrostatic FE solvers. The determination of steel ball bearing capacitances based on the combined numerical and experimental approach is included in Section IV. Section V presents the bearing voltage measurements and evaluates the bearing voltage reduction potential of several easy-to-implement methods. Section VI concludes the full paper.

II. PROPOSED FE MODEL OF ELECTRIC MACHINES COMBINED WITH DEC FOR BEARING VOLTAGE STUDY

This paper takes a 3-phase permanent-magnet synchronous machine (PMSM) as an example to model the bearing voltage and evaluates its reduction potential by employing insulated shaft and bearings, introducing additional insulation in the rotor, and changing the material of machine components, attempting to develop an effective and efficient modeling approach for bearing voltage and current study.

By "insulated shaft", the authors refer to the shaft whose diameter is reduced to fit in an insulation layer, e.g., plastic, between the shaft and inner ring of the bearing. "Insulated
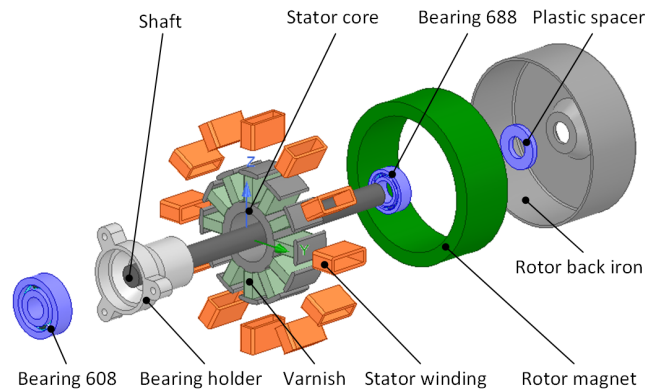

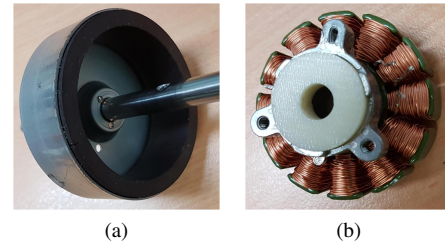Fig. 1. Exploded view of a PMSM with an outer rotor.

Fig. 2. PMSM under test: (a) outer rotor, (b) inner stator.

bearing" refers to the bearing whose outer surface of the outer ring and/or inner surface of the inner ring is E-coated or covered by plastic.

The construction of the 12-slot 10-pole (12s10p) PMSM illustrated in Fig. 1 has an outer rotor with surface-mounted bonded ferrite magnets and an inner stator with 12 concentrated tooth wound coils, as shown in Fig. 2.

There are 39 turns in each coil and two 0.352mm magnet wires in hand per turn. Both full ceramic bearings and steel ball bearings are used in the test. Photos of the full ceramic bearing 608 and steel ball bearing 608 are included in Fig. 3.

The DEC of the PMSM under study is developed for bearing voltage simulation, considering both the distribution
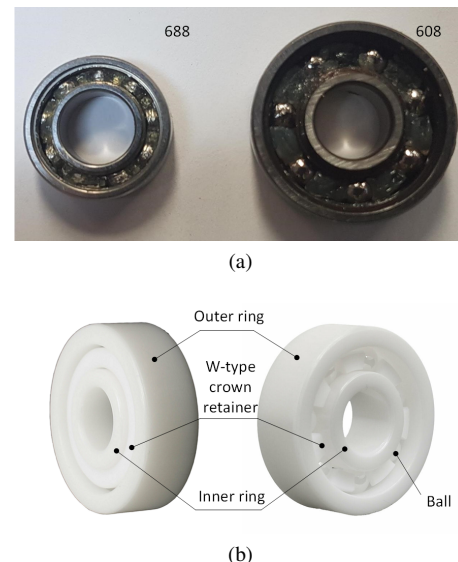

Fig. 3. Deep-groove ball bearings: (a) steel ball bearings with mental seal removed, (b) full ceramic bearing.
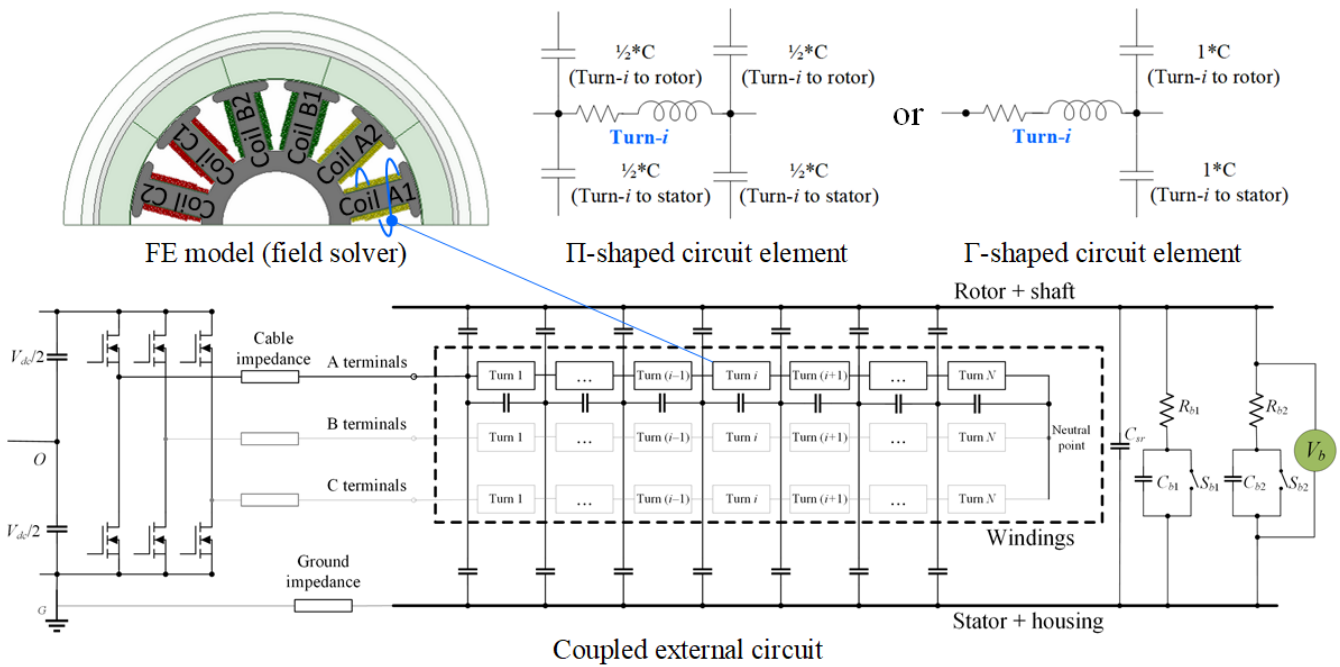
Fig. 4. DEC for the PMSM under test taking into account both the distribution of winding turns and frequency dependency of winding RL parameters. Windings are modeled turn by turn and each winding turn block in the external circuit corresponds to a turn in the FE model. Only capacitances related to Phase A coils are shown for clear illustration.
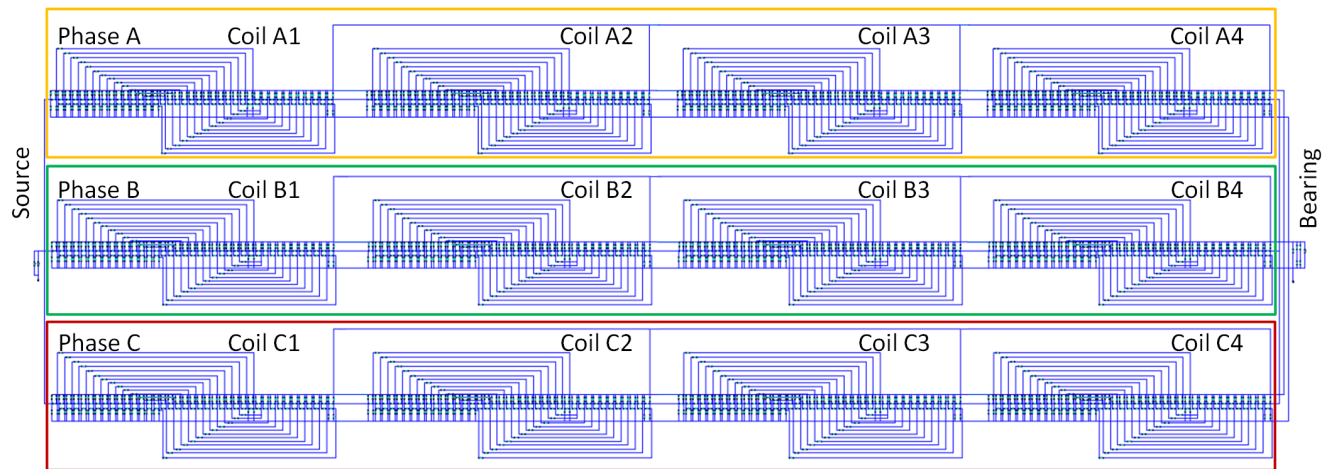

Fig. 5. An example of the external circuit used in the proposed method. Each phase has four coils in series and each coil has 39 turns. For the sake of clarity, only those dominating capacitors with coupling coefficients no smaller than 0.01 are modeled.

of winding turns and frequency dependency of winding RL parameters, as illustrated in Fig. 4. The bearing voltage waveform depends heavily on the inverter output, cable impedance, ground impedance, high-frequency parameters of the machine and bearing parameters. In order to show the effect of distributed parameters in transient simulations, the equivalent circuit includes details on winding turns.

One example of the detailed external circuit implemented in the proposed approach is shown in Fig. 5. Considering the symmetry of coils, the subcircuit of one coil can be reused to quickly construct the whole circuit. Scripts defining the nodes and their connections are recommended for more complicated machine windings. The source can be the 3-phase inverter as shown in Fig. 4 or a CMV. Capacitors are between coil turn terminals and rotor + shaft, between coil turn terminals and

stator, and between different coil turns.

For steady-state bearing voltage analysis, all the winding turns are equipotential and the equivalent circuit shown in Fig. 4 can be simplified to a pure capacitive LEC illustrated in Fig. 6, which is the traditional way to analyze bearing voltages. The constructions of stator and rotor in Fig. 2 show that the laminated stator core and the bearing holder are part of the same assembly and can be treated as a single node. Similarly, the rotor back iron and the shaft can be regarded as another node. The winding represents the third node since it is insulated from the stator core and rotor.

It is shown that the developed DEC model is consistent with the traditional LEC model in predicting the steady-state bearing voltage. The difference lies in that the DEC model can also be used to simulate the transients of bearing voltage,
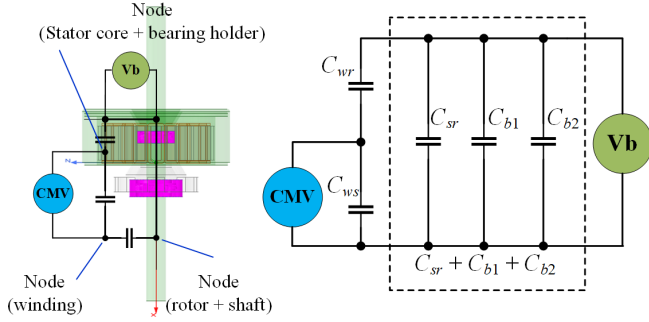
Fig. 6. The capacitive LEC for steady-state analysis of bearing voltage. C_{wr} is the lumped capacitance between stator winding and rotor, C_{sr} the lumped capacitance between stator core and rotor. C_{b1} and C_{b2} are the capacitances of bearing 1 and bearing 2, respectively. It is shown that in steady state, the bearing voltage is proportional to the CMV and the ratio is determined by C_{wr}, C_{sr}, and bearing capacitances. C_{ws} does not impact the voltage divider ratio.
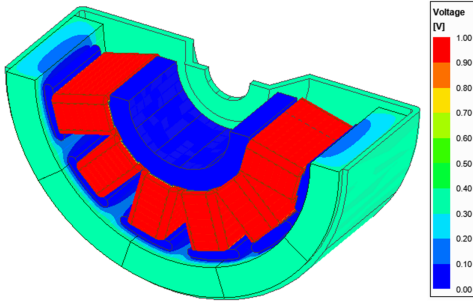

Fig. 7. Voltage distribution within the motor when 1V is applied to the stator winding and the stator core is grounded. There are in total 29.14 million tetrahedral elements and it took 35 hours to solve the problem on a high-performance PC with an 8-core Intel Xeon processor and 128GB RAM.

such as the ringing effect, which typically have much higher peaks than the steady-state values.

III. EXTRACTION OF MACHINE-RELATED CAPACITANCES

A. Electrostatic FEA for machine-related capacitances

The distributed resistance and inductance of the machine winding have been modeled inherently in the proposed approach. Only capacitances need to be extracted first and then incorporated into external circuits.

To capture the bearing voltage transients, machine windings need to be modeled in detail to consider the distribution effect of conductors. Each in-slot conductor or turn can be treated as an independent node to consider the voltage distribution along the wire. Capacitances in electric machines can be calculated using an electrostatic solver. The voltage distribution is visualized in Fig. 7.

The proposed method was implemented in Ansys Maxwell 2D magnetic transient solver. The conductor layout is shown in Fig. 8. Coils are assumed to be wound regularly with a needle winder starting from the bottom of the slot. There are 3 conductor layers and the two wires in hand are placed in pairs. The capacitance matrix shown in Fig. 9 has 4 traces highlighted by light colors. The two light blue traces denote capacitances between adjacent conductors from the same layer. The two yellow traces denote capacitances between conductors from adjacent layers.
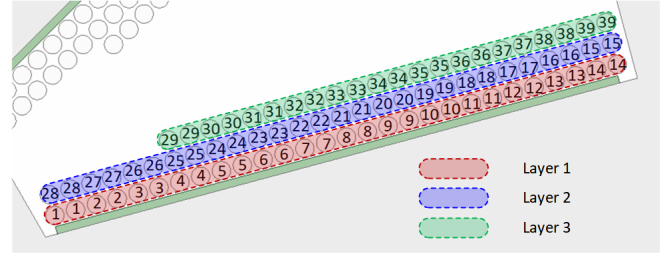

Fig. 8. Layout of turns in one coil of a phase winding. There are two 0.352mm wires in hand and coils are assumed to be wound regularly with a needle winder for the simplicity of modeling and analysis.
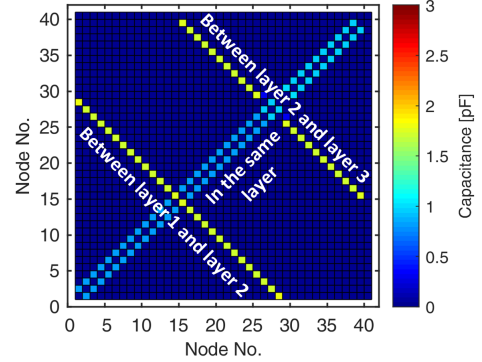

Fig. 9. Capacitance matrix for one coil of Phase B winding from FEA.

B. Measurement of machine-related capacitances

The winding-to-stator-core capacitance C_{ws}, stator-core-to-rotor-core capacitance C_{sr} and winding-to-rotor-core capacitance C_{wr} were calculated directly from 3D FEA shown in 7, including the bearings. Full ceramic bearings were used in the FE model to reduce the computation time. They were also measured from the motor assembly using an LCR meter Agilent U1733C. The individual capacitances were then calculated from the readings.

It should be noted that since the motor was in assembly when the capacitance measurements were conducted and two full ceramic bearings were used, the readings were not the individual capacitances. For example, when the two probes are placed on the winding terminal and the bearing holder, respectively, the capacitance reading is actually the individual capacitance C_{wr} in parallel with the series connection of C_{sr} and C_{wr}. A conversion from the capacitance readings to the individual capacitances is necessary. The readings were 290pF, 69pF, and 57pF. The individual capacitances calculated from the readings are tabulated in TABLE I.

Capacitors in electric machines are typically in pF to hundreds of pF level and measuring them using high-precision LCR meters is a common practice, as adopted by [8] and

TABLE I: Comparison of Calculated and Measured Capacitances in the Motor with Full Ceramic Bearings Made of Z_rO_2. The Dielectric Constant of Z_rO_2 Has a Small Impact on the FE predicted Capacitances.

Indiv. cap.	FEA ϵ_r =10 [pF]	FEA ϵ_r =23 [pF]	Meas. [pF]	Percentage Difference [%]
C_{ws}	316.3	316.2	286.2	+10.5
C_{sr}	64.9	66.9	65.1	-0.3/+2.8
C_{wr}	4.5	4.5	4.0	+12.5

[9]. In this paper, the measured machine-related capacitances are also confirmed by the FE calculations. The calculated and measured values tabulated in TABLE I show a maximum difference of 12.5%.

IV. DETERMINATION OF BEARING CAPACITANCES BASED ON A COMBINED NUMERICAL AND EXPERIMENTAL TECHNIQUE

Ball bearings are the most common type of bearing and extensively used in electric machines. According to the configuration of bearing rings, ball bearings are further classified as deep-groove ball bearings and angular contact ball bearings. According to the bearing material, ball bearings are categorized as steel ball bearings, hybrid ceramic ball bearings and full ceramic bearings. Shown in Fig. 3a and Fig. 3b are steel ball bearings with metal seal removed and full ceramic bearings.

A standard deep-groove ball bearing consists of a number of rolling balls and two concentric rings, which are made of steel for steel and hybrid ceramic ball bearings. In full ceramic ball bearings, all the balls and rings are made of ceramics, such as Silicon nitride (Si_3N_4) and Zirconium dioxide (ZrO_2). Besides the balls and rings, there are also ball retainers and grease seals in bearings. Ball retainers or ball cages are used to separate the balls, maintain the symmetrical radial spacing of balls and in most cases, hold the bearing together. Grease seals are used to protect bearings from excess grease loss and contamination. Both the cage and seal can be metals, introducing additional capacitances between the outer and inner rings.

A. Equivalent Circuit Model of Steel Ball Bearing

Based on the physical construction, the steel ball bearing can be modeled as a combination of capacitors, resistors, and voltage-controlled switches [1], as illustrated in Fig. 10, where R_{ir} and R_{or} represent the resistances of the inner and outer ring, respectively. There are N_b balls in parallel, each having an effective resistance $R_{b,i}$.

Considering each ball is immersed in the lubricant, each ball develops two capacitances, i.e., $C_{b-ir,i}$ and $C_{b-or,i}$, linking the inner and outer rings. Between balls, the inner and outer rings are separated by the lubricant and/or air, and an additional capacitance $C_{g,i}$ is formed. The ball retainer and seals, if made of metal, will also introduce capacitive coupling between the inner and outer races. Voltage-controlled switches are included to consider the possible breakdown of the lubricant. Once the voltage across the bearing lubricant film exceeds the threshold value, the electrical discharge machining will occur and the bearing turns into a resistor from an RC circuit. Combining the individual components results in a reduced-order bearing model, which consists of a resistance R_b in series with the parallel connection of a capacitance C_b and a voltage-controlled switch S_b.

For hybrid ceramic ball bearings and full ceramic bearings, the bearing model is a pure capacitor with mixed dielectrics, i.e., the ceramic, lubricant and air. Similar to steel ball bearings, metal retainers and seals will also introduce additional capacitances between inner and outer rings.
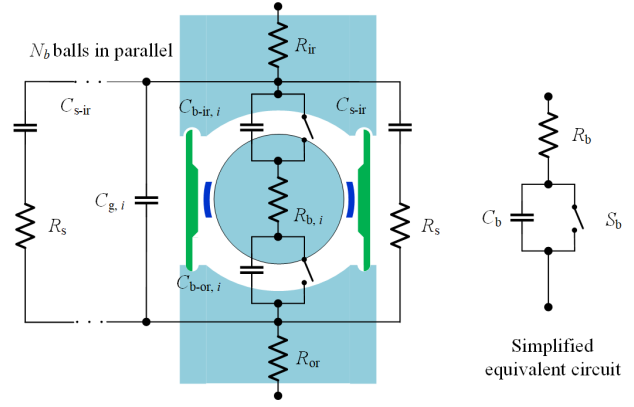

Fig. 10. Equivalent electric circuit model of steel ball bearings with metal ball retainers and seals
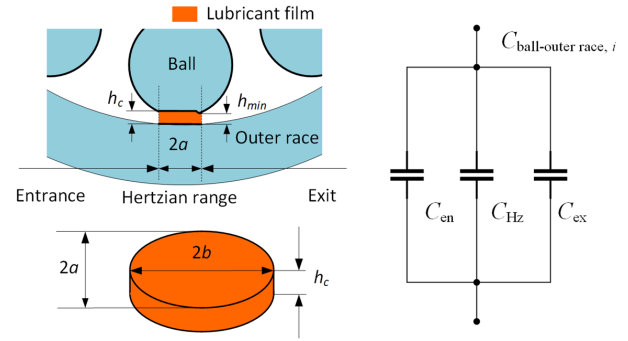

Fig. 11. Schematic of the lubricant film between the rolling ball and outer raceway, and the corresponding equivalent electric circuit.

For steel ball bearings, the key to calculate the capacitance between the inner and outer races lies in the estimation of the lubricant film thickness and contact area, which depend on the bearing geometry, lubricant property, lubrication status, speed and load. According to the Hertzian theory, the theoretical contact area is elliptical between a rolling ball and raceway, as illustrated in Fig. 11. The capacitance between each ball and the inner or outer raceway consists of three elements–the capacitance for the Hertzian ellipse C_{Hz}, the capacitance for the entrance C_{en} and the capacitance for the exit C_{ex}.

The central film thickness h_c can be calculated by the following formula [26]:

$$h_c = 2.69\overline{U}_r^{\,0.67}(\alpha E_{eq})^{0.53}\overline{W}^{-0.067}(1 - e^{-0.73k}), \quad (1)$$

where α is the viscosity-pressure coefficient. $\overline{U}_r$ and $\overline{W}$ are dimensionless velocity and load, respectively, defined by:

$$\overline{U}_r = \mu_0 U_r (E_{eq} R_x)^{-1}, \quad (2)$$

$$\overline{W} = W(E_{eq} R_x^2)^{-1}, \quad (3)$$

where U_r is the rolling velocity, μ_0 the viscosity of the lubricant at atmospheric pressure and bearing operating temperature, W the load on one rolling ball. E_{eq} is the equivalent modulus of elasticity. In the calculation, $\alpha = 2.3 \times 10^{-8}$ m²/N, $\mu_0 = 0.01$ Ns/m², and $E_{eq} = 2.25 \times 10^{11}$ N/m², were used. It should be noted that these typical values for the lubricant and steel were used to give reasonable estimations of the capacitance components. The permittivities were then determined by the least square regression analysis of measured
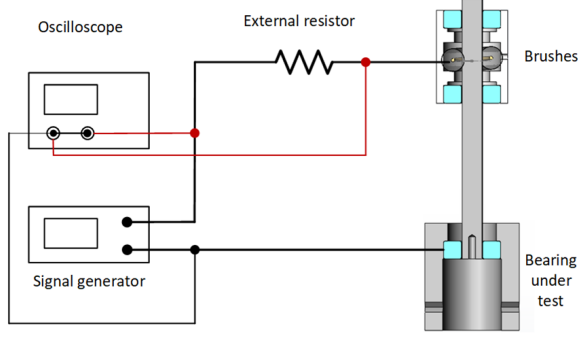
Fig. 12. Schematic diagram of the bearing capacitance measurement

TABLE II: Contact angle, film thickness and capacitance breakdown at 1,200r/min with different axial loads. Regression analysis shows the optimal coefficients for the bearing under test are: $\epsilon_f = 1.0$, $\epsilon_e = 1.0$ and $C_{oth} = 52.0$pF. Each measurement was done quickly and there was a long break between two consecutive measurements to keep the lubricant temperature constant.

Axial load [N]	$C_{Hz,i}$ [pF]	$C_{en,i} + C_{ex,i}$ [pF]	Calc. C_b [pF]	Meas. C_b [pF]	Diff. [%]
0	0.45 0.39	4.65 5.49	71.1	78.2	-9.1
49	8.28 6.31	4.66 5.49	95.2	95.7	-0.5
98	12.08 9.22	4.66 5.49	106.8	99.2	+7.7

TABLE III: Ratings and specifications of the PMSM under test.

Rated torque [Nm]/speed [r/min]	0.13/2480
Total OD/stator ID [mm]	61/18
Dc bus voltage [V]	24
Air-gap/stack length [mm]	0.3/14
Max. phase current [Arms]	2.5

bearing capacitances under various load conditions. It has been assumed that the temperature of the lubricant film was constant and special attention should be paid during the measurement to keep temperature stable.

The three capacitances can then be calculated from the following two equations derived from the parallel-plate capacitor model:

$$C_{Hz,i} = \epsilon_0 \epsilon_f \frac{\pi ab}{h_c}, \tag{4}$$

$$C_{en,i} + C_{ex,i} = 2\pi\epsilon_0\epsilon_e \int_a^r \frac{\frac{b}{a}x}{h_c + h(x)}dx, \quad h(r) = 100h_c, \tag{5}$$

where ϵ_0 is the vacuum dielectric constant, ϵ_f and ϵ_e the relative dielectric constant of lubricant film in Hertzian area and entrance/exit area, respectively. Radii of the ellipse are denoted by a and b. The distance between the outer surface of the ball and the inner surface of the ring at x is denoted by $h(x)$.

The resulting capacitance of the steel ball bearing can be written as:

$$C_b = \sum_{n=1}^{N_b} C_{Hz,i} + (C_{en,i} + C_{ex,i}) + C_{oth}, \tag{6}$$

where C_{oth} accounts for the additional capacitances introduced by metal seals and/or ball retainer.

B. Experimental Measurements for Coefficient Determination

Equation (6) includes three main unknown parameters, i.e., ϵ_f, ϵ_e and C_{oth}, which are difficult to be accurately determined directly in practice, even when the operating temperature, bearing speed and load are given. To determine them, at least 3 experimental measurements of the capacitance are required for a basic least squares regression analysis. More measurement data will improve the accuracy and provide better predictions of bearing capacitance under various operating conditions.

The schematic diagram of the bearing capacitance measurement is shown in Fig. 12. The bearing under test was installed on a PVC-U pressure pipe vertically so that pure axial load can be applied. The brush labeled in Fig. 12 is a rotating connector Mercotac 230. The capacitance was calculated from the measured voltage and current waveforms instead of direct measurement by an LCR meter, as detailed in [25].

The signal generator produces a step voltage signal or a pure sinusoidal voltage signal. An external high-precision resistor with a constant resistance is connected in series with the

bearing under test through a rotating connector, i.e., the brush in Fig. 12. The amplitude of the applied voltage signal is set to a relatively low value to avoid the lubricant film breakdown. The time constant and the ratio between the bearing voltage and the step voltage input can be measured to calculate the bearing capacitance C_b and resistance R_b, as demonstrated in [23]. Alternatively, the waveforms for the bearing voltage and the high-frequency sinusoidal voltage input can be recorded by an oscilloscope and used to calculate the bearing capacitance and resistance.

The measured capacitances of a deep-groove steel ball bearing with two metal seals under 0N, 49N and 98N additional axial loads are shown in TABLE II. This type of bearing requires a load of at least 40N for operation.

Based on equation (6) and the measured results, the optimal ϵ_f, ϵ_e and C_{oth} can be determined by minimizing $\left(C_b^{calc} - C_b^{meas}\right)^2$ with three constraints: $1 \leq \epsilon_f \leq 5$, $1 \leq \epsilon_e \leq 5$, and $C_{oth} \geq 0$. With the optimized coefficients, the calculated bearing capacitance and its breakdown are tabulated in TABLE II for comparison.
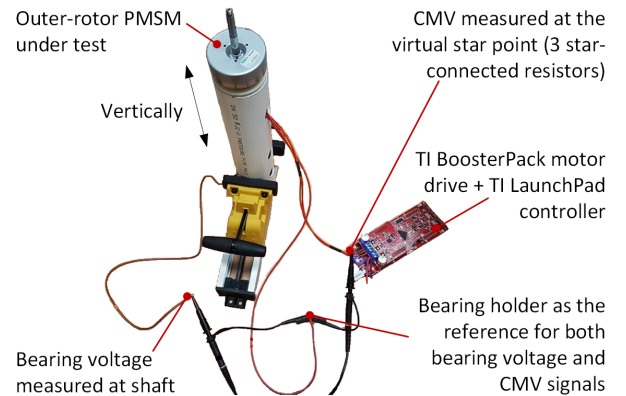

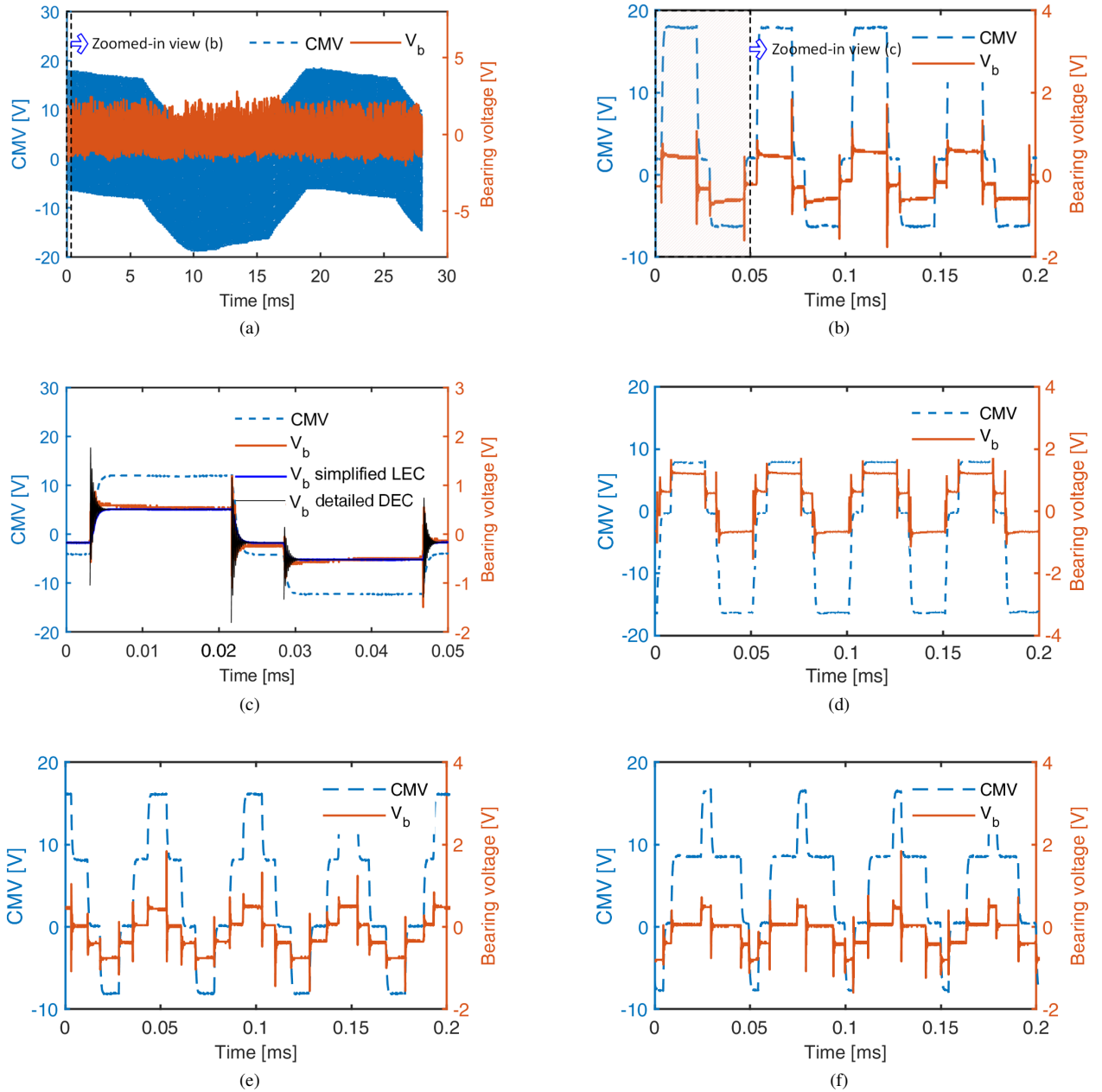Fig. 13. Test setup for bearing voltage measurement.

Fig. 14. Measured CMV and bearing voltage for: (a) steel ball bearing at 1,200r/min in a long period of time, (b) zoomed-in view of (a), (c) zoomed-in view of (b) in comparison with simulation results from both the simplified LEC and detailed DEC models, (d) full ceramic bearing at 1,200r/min, (e) steel ball bearing at 2,400r/min, (f) steel ball bearing at 3,360r/min.

V. BEARING VOLTAGE MEASUREMENT AND REDUCTION METHODS

A. Bearing voltage measurement

The test setup for bearing voltage measurement shown in Fig. 13 includes the outer-rotor PMSM under test driven by a TI BoosterPack motor drive and a TI LaunchPad controller. The PMSM was installed on a PVC-U pressure pipe vertically so that both bearings have only axial loads. Two Pico differential probes were used to measure the CMV and bearing voltage with the bearing holder as the reference point. Ratings and specifications of the PMSM are tabulated in TABLE III.

Experimental tests were conducted on the PMSM under study at 1,200r/min with a fixed dc bus voltage of 24V. The space vector PWM (SVPWM) based field-oriented control

was employed to control the motor speed with a switching frequency of 20kHz. The CMV and bearing voltage waveforms were recorded by an oscilloscope with a sampling frequency of 1GHz, as shown in Fig. 14. The bearing voltage shows similar waveform to the CMV, except the ringing at the rising and falling edges and the offsets. The mismatch of zero stages was caused by floating the bearing holder during the measurement. Therefore, the pulsation of CMV is expected, as shown in Fig. 14a.

In order to have a fair comparison with simulated waveforms, the reference has to be adjusted. Fig. 14c shows the adjusted CMV and bearing voltage from measurement, together with the simulated ones by the simplified LEC and detailed DEC. It can be seen that though both the simplified

LEC and detailed DEC can be used to simulate the steady-state voltages, the detailed DEC also predict the transients, which is usually much higher than the steady-state values.

It can be seen that the bearing voltage mirrors the CMV very well in the tested speed range from 1,200r/min to 3,360r/min. Voltage ringing is observed at the rising and falling edges of the bearing bearing voltage, which is introduced by the distributed winding resistances and inductances.

B. Bearing voltage reduction by insulated shaft and bearings

The potential of bearing voltage reduction by insulating the bearing from the shaft and/or bearing holder was studied based on the developed FE model with DEC. The dielectric constant of the E-coating layer and plastic are assumed at the typical value of 3.0.

A layer of insulation was inserted between the inner ring of bearing 608 and shaft or the outer ring of bearing 608 and bearing holder. The influence of the insulation thickness on the voltages of bearing 608 and 688 shown in Fig. 15 indicates that with the increase of the insulation thickness, the voltage of the insulated bearing was reduced but the voltage of the non-insulated bearing increased slightly. The capacitive LEC shown in Fig. 6 can be used to explain this phenomenon intuitively. By insulating bearing 1, an additional capacitor is introduced to be in series connection with C_{b1}. As a result, the voltage across C_{b2} will be increased assuming the CMV is constant. An 80% and 55% voltage reduction can be achieved by insulating the inner ring and outer ring, respectively. Insulating bearing 688 shows similar trends.

Fig. 16 shows that both bearing voltages can be reduced by insulating bearing 608 and bearing 688 at the same time. With a 1-mm thick insulation layer inserted between the inner rings and shaft, the bearing voltages can be reduced by around 70%. In addition, insulating the inner rings reduces more bearing voltage due to the smaller facing surfaces. This is because there is voltage divider effect between the capacitor introduced by the insulation layer and the bearing. The capacitor formed by the insulator, the shaft and the inner ring of the bearing has a smaller capacitance value due to the smaller surface area, so the corresponding impedance is larger.

C. Bearing voltage reduction by inserting additional insulation

In addition to insulated shaft and/or bearings, other possible bearing voltage reduction approaches were also studied based on the proposed FE model combined with external circuits. It has been predicted from the FE simulation that introducing an additional 1mm-thick insulation layer between the rotor hub and shaft can also help reduce the voltages of both bearing simultaneously by 89%. Fig. 17 shows the bearing voltages before and after inserting a 1mm-thick insulation layer between the rotor hub and shaft, indicating a reduction of 77%. The modified PMSM rotor is shown in Fig. 18a, where the additional insulation layer is highlighted.
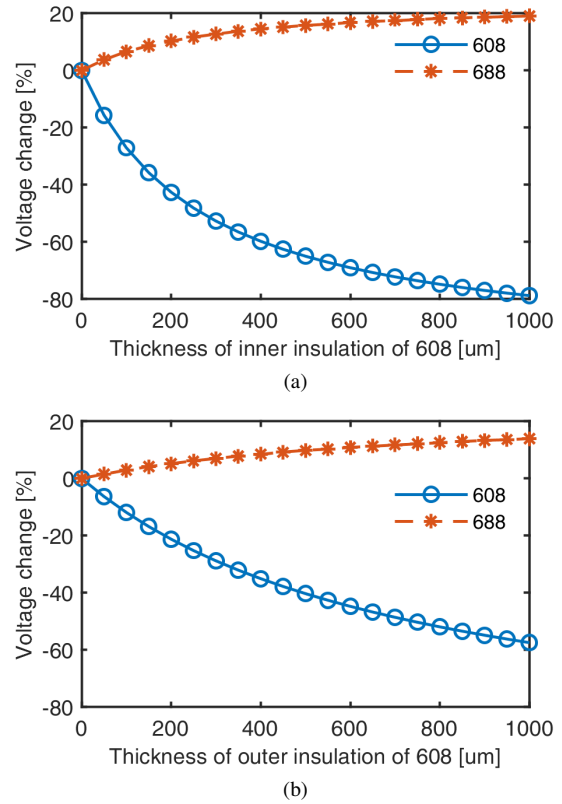

Fig. 15. Bearing voltage reduction versus the thickness of insulation between: (a) the inner ring of bearing 608 and shaft, (b) the outer ring of bearing 608 and bearing holder. Inner rings have smaller surfaces and therefore produces larger additional impedance and voltage reduction.
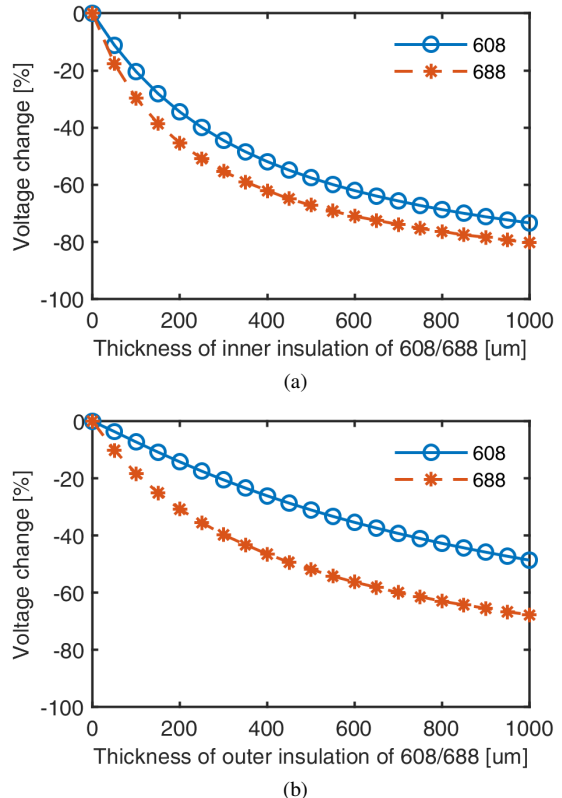

Fig. 16. bearing voltage reduction versus thickness of insulation layers on: (a) inner surfaces of both bearing 608 and 688, (b) outer surfaces of both bearing 608 and 688. Voltages of bearing 608 and 688 can be reduced effectively by insulating the inner or outer surfaces of both bearings simultaneously.
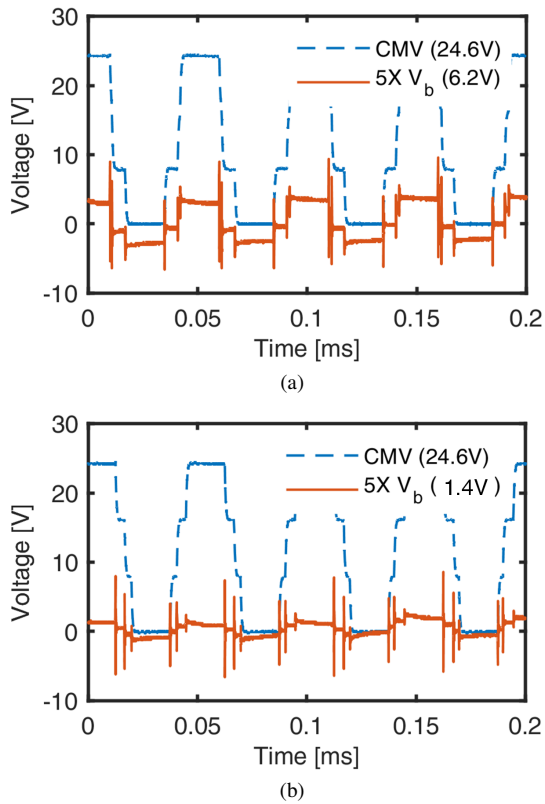
Fig. 17. Measured bearing voltage of (a) before and (b) after inserting an additional layer of insulation between the rotor hub and shaft.
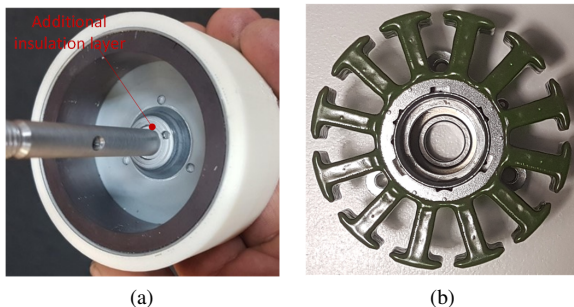

Fig. 18. Modified PMSM: (a) rotor with a 1mm-thick insulation layer inserted, (b) stator core with the bearing holder and coils removed.

D. Bearing voltage reduction by changing the material of bearing holder

The bearing voltage can also be reduced by replacing the original bearing holder made of aluminum with a plastic one. The bearing voltage reduction simulated by the proposed model at various speeds is shown in Fig. 19. It is predicted that the voltage across bearing 608 will be reduced more than 95% and a reduction of 50% is expected for the bearing 688.

VI. Conclusion

This paper presents a method to model the bearing voltage in electric machines using electromagnetic FEA and measured bearing capacitance, based on which the bearing voltage reduction potential of using insulated shaft and bearings is evaluated. To improve the accuracy of bearing voltage prediction, a procedure to determine the bearing capacitance by
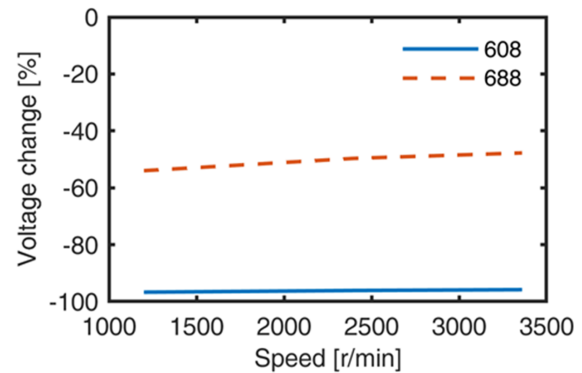

Fig. 19. Bearing voltage reduction by using a plastic bearing holder.

combining numerical calculations and experimental measurements is developed.

It is shown that in order to track the transients in bearing voltages when the motor is running, FE models with detailed winding information are required to take into account the distribution and high-frequency effect of machine windings. For steady-state analysis, the simplified equivalent circuit with lumped capacitance parameters may be used.

It is also shown that with the combined numerical and experimental approach, the percentage error for bearing capacitance calculations can be reduced. Insulating a single bearing can reduce the voltage on the insulated bearing but will adversely increase the voltage on the non-insulated bearing. To reduce the voltage of both bearings, it is recommended to insulate the inner rings of both bearings. The voltage reduction achieved by insulated shaft/bearings depends on the size of motors and bearings, and a maximum voltage reduction of 70% is expected in the PMSM under study.

In industrial applications, it is important to keep a balance between the electromagnetic performance and mechanical considerations, so the mechanical properties of the insulation layer should be carefully considered when using this method for machines of different ratings and sizes. Inserting additional insulation between the rotor hub and shaft, and replacing the metal bearing holder with a plastic one are also effective ways to reduce voltages of both bearings.

The proposed bearing voltage modeling approach and the combined numerical and experimental determination of bearing capacitance can also be directly applied to other machines. The effectiveness and influence of high transient bearing voltage peaks are the next step of our ongoing research.

VII. Acknowledgment

References

[1] J. M. Erdman, R. J. Kerkman, D. W. Schlegel, and G. L. Skibinski, "Effect of PWM inverters on AC motor bearing

currents and shaft voltages," *IEEE Trans. Ind. Appl.*, vol. 32, no. 2, pp. 250–259, Mar. 1996.

[2] D. Busse, J. Erdman, R. J. Kerkman, D. Schlegel, and G. Skibinski, "Bearing currents and their relationship to PWM drives," *IEEE Trans. Power Electron.*, vol. 12, no. 2, pp. 243–252, March 1997.

[3] A. von Jouanne, H. Zhang, and A. K. Wallace, "An evaluation of mitigation techniques for bearing currents, EMI and overvoltages in ASD applications," *IEEE Trans. Ind. Appl.*, vol. 34, no. 5, pp. 1113–1122, Sep. 1998.

[4] A. Muetze and A. Binder, "Practical rules for assessment of inverter-induced bearing currents in inverter-fed AC motors up to 500 kW," *IEEE Trans. Ind. Electron.*, vol. 54, no. 3, pp. 1614–1622, 2007.

[5] A. von Jouanne, R. Collin, M. Stephens, Y. Miao, B. Thayil, C. Li, E. Agamloh, and A. Yokochi, "Motor bearing current characterization in SiC-based variable frequency drive applications," in *Proc. IEEE Energy Convers. Congr. Expo. (ECCE)*, 2020, pp. 2718–2725.

[6] A. Binder and A. Muetze, "Scaling effects of inverter-induced bearing currents in AC machines," *IEEE Trans. Ind. Appl.*, vol. 44, no. 3, pp. 769–776, May 2008.

[7] T. Plazenet, T. Boileau, C. Caironi, and B. N.-Mobarakeh, "A comprehensive study on shaft voltages and bearing currents in rotating machines," *IEEE Trans. Ind. Appl.*, vol. 54, no. 4, pp. 3749–3759, Jul. 2018.

[8] Y. Isomura, K. Yamamoto, S. Morimoto, T. Maetani, A. Watanabe, and K. Nakano, "Study of the further reduction of shaft voltage of brushless DC motor with insulated rotor driven by PWM inverter," *IEEE Trans. Ind. Appl.*, vol. 50, no. 6, pp. 3738–3743, Nov. 2014.

[9] S. Lee, J. Park, C. Jeong, S. Rhyu, and J. Hur, "Shaft-to-frame voltage mitigation method by changing winding-to-rotor parasitic capacitance of IPMSM," *IEEE Trans. Ind. Appl.*, vol. 55, no. 2, pp. 1430–1436, Mar. 2019.

[10] J. Adabi, F. Zare, A. Ghosh, and R. D. Lorenz, "Calculations of capacitive couplings in induction generators to analyse shaft voltage," *IET Power Electron.*, vol. 3, no. 3, pp. 379–390, May 2010.

[11] J. Park, T. R. Wellawatta, S. Choi, and J. Hur, "Mitigation method of the shaft voltage according to parasitic capacitance of the PMSM," *IEEE Trans. Ind. Appl.*, vol. 53, no. 5, pp. 4441–4449, Sep. 2017.

[12] M. Schuster, D. Masendorf, and A. Binder, "Two PMSMs and the influence of their geometry on common-mode bearing currents," in *Proc. Int. Conf. Electr. Mach. (ICEM)*, Sep. 2016, pp. 2126–2132.

[13] M. Asefi and J. Nazarzadeh, "Survey on high-frequency models of PWM electric drives for shaft voltage and bearing current analysis," *IET Electr. Syst. Transport.*, vol. 7, no. 3, pp. 179–189, 2017.

[14] A. Muetze and A. Binder, "Calculation of influence of insulated bearings and insulated inner bearing seats on circulating bearing currents in machines of inverter-based drive systems," *IEEE Trans. Ind. Appl.*, vol. 42, no. 4, pp. 965–972, 2006.

[15] D. Busse, J. Erdman, R. Kerkman, D. Schlegel, and G. Skibinski, "An evaluation of the electrostatic shielded induction motor: a solution for rotor shaft voltage buildup and bearing current," *IEEE Trans. Ind. Appl.*, vol. 33, no. 6, pp. 1563–1570, 1997.

[16] S. Lee, M. Liu, W. Lee, and B. Sarlioglu, "Comparison of high-frequency impedance of AC machines with circumferential and toroidal winding topologies for SiC MOSFET machine drives," in *Proc. IEEE Energy Convers. Congr. Expo. (ECCE)*, 2020, pp. 3572–3579.

[17] S. Quabeck, V. Grau, and R. W. De Doncker, "Modeling and mitigation of bearing currents in electrical traction drives," in *Proc. Int. Conf. Electr. Mach. Syst. (ICEMS)*, 2020, pp. 1101–1106.

[18] M. S. Toulabi, L. Wang, L. Bieber, S. Filizadeh, and J. Jatskevich, "A universal high-frequency induction machine model and characterization method for arbitrary stator winding connections," *IEEE Trans. Energy Convers.*, vol. 34, no. 3, pp. 1164–1177, 2019.

[19] V. Mihaila, S. Duchesne, and D. Roger, "A simulation method to predict the turn-to-turn voltage spikes in a PWM fed motor winding," *IEEE Trans. Dielectr. Electr. Insul.*, vol. 18, no. 5, pp. 1609–1615, 2011.

[20] S. Sundeep, J. Wang, and A. Griffo, "Prediction of transient voltage distribution in inverter-fed stator winding, considering mutual couplings in time domain," in *Prof. IEEE Energy Convers. Congr. Expo. (ECCE)*, 2020, pp. 517–524.

[21] Y. Xie, J. Zhang, F. Leonardi, A. R. Munoz, M. W. Degner, and F. Liang, "Modeling and verification of electrical stress in inverter-driven electric machine windings," *IEEE Trans. Ind. Appl.*, vol. 55, no. 6, pp. 5818–5829, 2019.

[22] O. Magdun and A. Binder, "Calculation of roller and ball bearing capacitances and prediction of EDM currents," in *in Proc. IEEE Ind. Electron. Annu. Conf.*, Nov 2009, pp. 1051–1056.

[23] E. Wittek, M. Kriese, H. Tischmacher, S. Gattermann, B. Ponick, and G. Poll, "Capacitances and lubricant film thicknesses of motor bearings under different operating conditions," in *Proc. Int. Conf. Electr. Mach. (ICEM)*, Sep. 2010, pp. 1–6.

[24] P. Han, G. Heins, D. Patterson, M. Thiele, and D. M. Ionel, "Evaluation of bearing voltage reduction in electric machines by using insulated shaft and bearings," in *Proc. IEEE Energy Convers. Congr. Expo. (ECCE)*, 2020, pp. 5584–5589.

[25] ——, "Combined numerical and experimental determination of ball bearing capacitances for bearing current prediction," in *Proc. IEEE Energy Convers. Congr. Expo. (ECCE)*, 2020, pp. 5590–5594.

[26] A. Harnoy, *Bearing Design in Machinery: Engineering Tribology and Lubrication*. CRC Press, 2002.

Peng Han (Senior Member, IEEE) received the B.Sc. and Ph.D. degrees in Electrical Engineering from the School of Electrical Engineering, Southeast University, Nanjing, China, in 2012 and 2017, respectively.

From November 2014 to November 2015, he was a joint Ph.D. student funded by China Scholarship Council with the Department of Energy Technology, Aalborg University, Aalborg, Denmark, where he focused on the brushless doubly-fed machines for wind energy conversion and high power drive. He was a postdoctoral researcher with the Center for High Performance Power Electronics (CHPPE), Department of Electrical and Computer Engineering, The Ohio State University, and later the SPARK Laboratory, Department of Electrical and Computer Engineering, University of Kentucky. He is currently with Ansys, Inc. as a Senior Application Engineer. His current research interests include electric machines, machine drives, power electronics and renewable energy.

Greg Heins (Member, IEEE) received the B.Eng. (Hons.) degree in Mechanical Engineering and the University Medal from the University of New South Wales, Sydney, NSW, Australia, in 2000, and the Ph.D. degree in Mechatronics, Robotics, and Automation Engineering from Charles Darwin University, Darwin, NT, Australia, in 2008.

He is currently the Head of the Research and Development for Regal Beloit Corporation, Asia Pacific, Rowville, VIC, Australia. He was previously a Manufacturing Engineer with the Robert Bosch Australia and a Senior Lecturer with Charles Darwin University. His research interests include the design, control, and manufacture of electric motors, vibration analysis, system modeling and identification.

Dr. Heins was the recipient of the Australian Learning and Teaching Citation for Outstanding Contributions to Student Learning in 2011.

Dean Patterson (Life Fellow, IEEE) was born and raised in Adelaide, SA, Australia. He received the Ph.D. degree in Electrical Engineering from the University of Adelaide, Adelaide, SA, Australia.

He moved to an Embryonic University, now Charles Darwin University, Darwin, NT, Australia, where he was responsible for the four-year undergraduate degree program, the graduate degree program, and the establishment of a research focus. He was recently awarded a Doctor of Science "honoris causa" by Charles Darwin University. He has been active in the Power Electronics Society since 1989, on its AdCom since 1992, and has served as President of PELS. In 2001, he moved to the USA, to the University of South Carolina, Columbia, SC, USA, as a Research Professor, and in 2004, was invited to the University of Nebraska Lincoln, Lincoln, NE, USA. His spin-off company from the Northern Territory University, specializing in very high efficiency electric machines, was bought in 2006 by FASCO, who were more recently acquired by Regal Beloit Corporation. He is currently the Chief Scientist with the Regal Beloit Corporation Asia Pacific, Rowville, VIC, Australia.

Mark Thiele (Member, IEEE) received the B.Eng. (Mech.) degree from the Swinburne University of Technology, Melbourne, Australia, in 1995 and the Ph.D. (Mech.) degree from Charles Darwin University, Darwin, Australia, in 2014.

After he received the B.Eng. degree, he was with the automotive industry for nine years and then lectured in mechanical engineering with Charles Darwin University for six years. He is currently a Senior Electromagnetic Design Engineer with Regal Beloit Australia, Rowville, VIC, Australia. His research interests focus on the causes of acoustic noise, especially manufacturing related, in permanent-magnet machines.

Dan M. Ionel (Fellow, IEEE) is Professor of Electrical Engineering and the L. Stanley Pigman Chair in Power at the University of Kentucky, Lexington, KY, where he is also the Director of the Power and Energy Institute of Kentucky (PEIK) and of the SPARK Laboratory. He previously worked in industry, most recently as Chief Engineer for Regal Beloit Corp., Grafton, WI, USA, and, before that, as the Chief Scientist for Vestas Wind Turbines. Concurrently, he was also a Visiting and Research Professor with the University of Wisconsin and Marquette University in Milwaukee, WI. Dr. Ionel contributed to technology developments with long lasting industrial impact, holds more than 35 patents, published more than 200 papers, and co-authored 3 books. His research has been supported directly by industry, and by NSF, NIST, DOE, and NASA.

He received the M.Eng. and Ph.D. degrees in electrical engineering from the Polytechnic University of Bucharest, Bucharest, Romania. His doctoral program included a Leverhulme Visiting Fellowship with the University of Bath, Bath, U.K., and later he was a Postdoctoral Researcher with the SPEED Laboratory, University of Glasgow, Glasgow, U.K.

Dr. Ionel is an IEEE Fellow and a recipient of the IEEE PES Veinott Award. He was the Inaugural Chair of the IEEE Industry Applications Society Renewable and Sustainable Energy Conversion Systems Committee, an Editor for the IEEE Transactions on Sustainable Energy, the Chair of the IEEE PES MSC and of the IEEE WG 1812, the Technical Program Chair of 2015 IEEE ECCCE and the General Chair of the 2017 IEEE IEMDC. He is the Editor-in-Chief of the Electric Power Components and Systems Journal, and the Chair of the Steering Committee for the IEEE IEMDC Conferences.